Electronic Supplementary Material (ESI) for Journal of Materials Chemistry A.
This journal is © The Royal Society of Chemistry 2019

Electronic Supplementary Information

Micropore-confined amorphous SnO_2 subnanoclusters as robust anode materials for Na-ion capacitors

Jin Niu,[a,b] Jingjing Liang,[a,b] Ang Gao, Meiling Dou,[a,b] Zhengping Zhang,[a,b,*] Xia Lu,[b,c,*] Feng Wang[a,b,*]

[a]State Key Laboratory of Chemical Resource Engineering, Laboratory of Electrochemical Process and Technology for materials, Beijing University of Chemical Technology, Beijing 100029, China

[b]Beijing Advanced Innovation Center for Soft Matter Science and Engineering, Beijing University of Chemical Technology, Beijing 100029, P. R. China

[c]School of Materials, Sun Yat-sen University, Guangzhou 510275, P. R. China

* Corresponding Authors.

E-mail: wangf@mail.buct.edu.cn (F. Wang); luxia3@mail.sysu.edu.cn (X. Lu); zhangzhengping@mail.buct.edu.cn (Z. Zhang).

Supplementary details for sample preparation

GO was synthesized by the method used in our previous work.[1] HPCNS-800 was prepared by pyrolyzing HPCNS at 800 °C for 1 h in an Ar atmosphere (heating rate: 5 °C min^{-1}). PCNS and rGO were obtained by heat-treating HPCNS and GO, respectively, at 400 °C for 1 h in an Ar atmosphere (heating rate: 5 °C min^{-1}). The cathode material (HPC, derived from cattle bone) for NIC was prepared by the method used in our previous work.[2]

The mass ratio of HPCNS to $SnCl_2 \cdot 2H_2O$ was determined by the available micropore volume of HPCNS due to the strong adsorption and nanoconfined effect of micropores. As shown in Table S1, the micropore volume of HPCNS was calculated to be 0.112 $cm^3\ g^{-1}$. Ideally, ~0.778 g of SnO_2 (with a theoretical density of 6.95 g cm^{-3}) could be filled in the micropores for 1 g of HPCNS. Correspondingly, ~1.16 g of $SnCl_2 \cdot 2H_2O$ should be used as the Sn precursor. Thus, the mass ratio of $SnCl_2 \cdot 2H_2O$ to HPCNS was estimated to be 6:5.

C-SnO_2@rGO and C-SnO_2@PCNS-800 were prepared using GO and HPCNS-800 as the support materials, respectively, under the same synthetic conditions as for A-SnO_2@PCNS. C-SnO_2@PCNS-2.4 was prepared using an $SnCl_2 \cdot 2H_2O$ to HPCNS precursor ratio of 12:5 under the same synthetic conditions as for A-SnO_2@PCNS.

Supplementary details for First-principles calculation method

A 2 × 2 × 2 supercell containing 48 atoms for SnO_2 (Space Group: $P4_2mnm$) was adopted for geometry optimizations as shown in Fig. S13. Three crystalline SnO_2 models (Fig. S13a-c) were constructed, including pristine SnO_2, SnO_2 with expansile rate of 5 % and SnO_2 with expansile rate of 10 %. The calculated energy for optimized SnO_2 structures with different expansion ratios were shown in Fig. S13d. Supercells with a range from 48 to 64 atoms (such as 56 atoms in $Na_{0.5}SnO_2$) were established for thermodynamic simulations of Na_xSnO_2 ($0 < x < 1$) with different Na contents. The unit cells of Na_2O based on *Fm***Error!***m* and Sn based on *Fm***Error!***ms* were used for thermodynamic simulations. The per

formula unit energy for SnO_2, Na_2O, and Sn with different space groups based on DFT calculations were shown in Table S4. The relative formation energy of intermediates during the sodiation processes of SnO_2 with different degrees of expansion were shown in Fig. S14.

To explore the Na-ion diffusion in the interface between Sn and carbon materials, the interface structure of defect graphene and the Sn surface was constructed. We modelled a Sn surface containing 8 Sn atoms and the graphene lattice with a 4 × 4 supercell (Fig. S15a). In order to study the effects of N doping on Na diffusion in the interface of carbon materials and Sn, we employed four defect graphene models (including graphene without N doping and with graphitic, pyridinic, and pyrrolic N doping) as shown in Fig. S15b-e. The thickness of the vacuum was set to 15 Å for the interface of graphene and Sn.

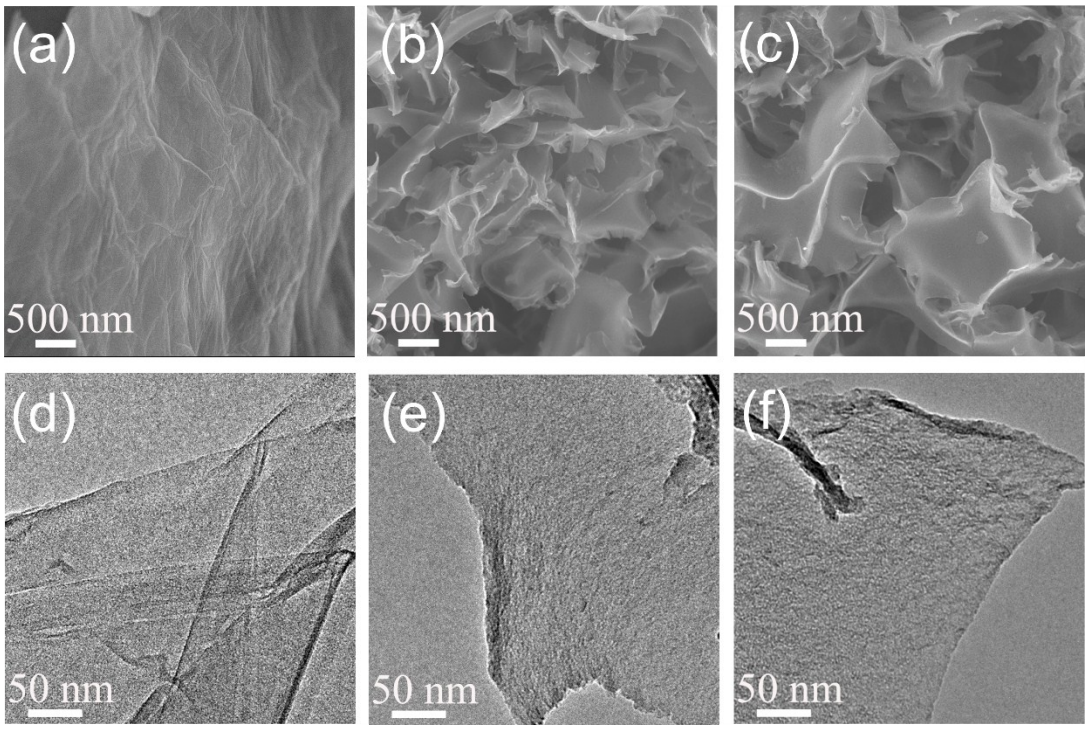

Figure S1. SEM images of (a) GO, (b) HPCNS and (c) HPCNS-800. TEM images of (d) GO, (e) HPCNS and (f) HPCNS-800.

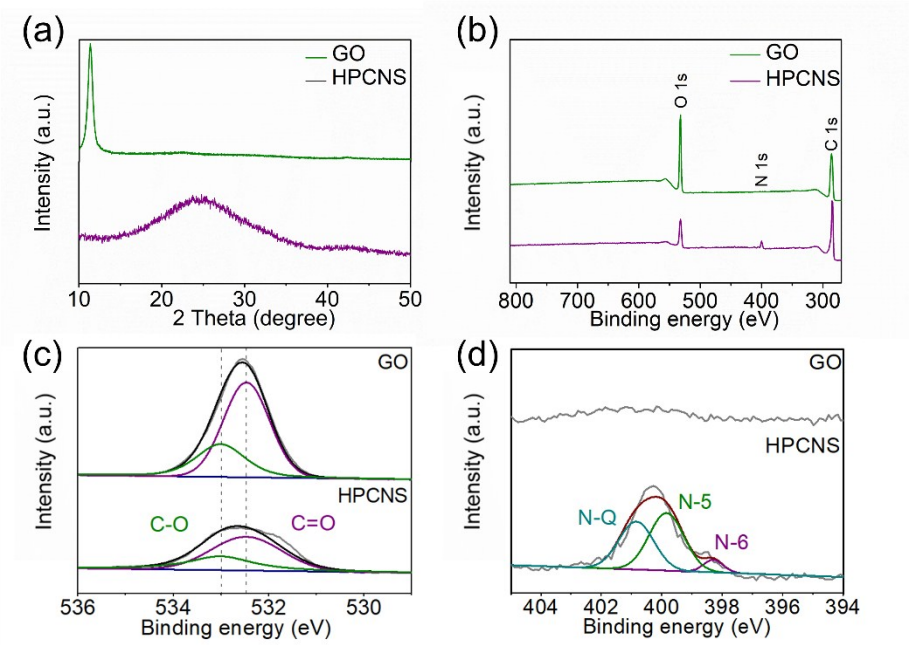

Figure S2. (a) XRD patterns of GO and HPCNS. (b) XPS spectra of GO and HPCNS. High-resolution XPS spectra of (c) O 1s and (d) N 1s for GO and HPCNS.

The high-resolution O1s XPS spectra for GO and HPCNS were deconvoluted into two individual component peaks as follows: C-O (531.6 eV) and C=O (533.3 eV).[3] The high-resolution N1s XPS spectrum for HPCNS was deconvoluted into three individual component peaks as follows: pyridinic-N (N-6, 398.2 eV), pyrrolic-N (N-5, 399.9 eV) and quaternary-N (N-Q, 401.0 eV).[3, 4]

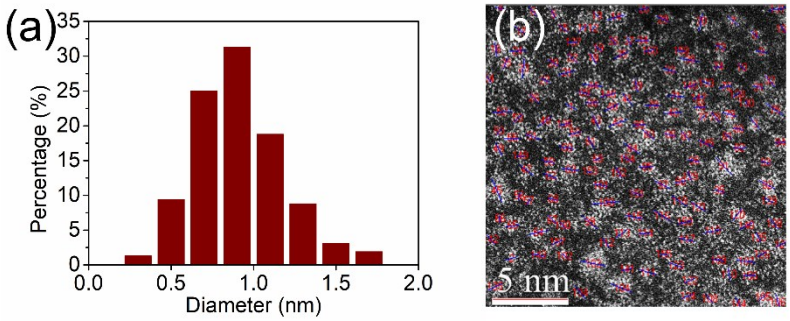

Figure S3. (a) Cluster size distribution of A-SnO_2 that was determined by 160 clusters shown in (b) the HAADF STEM images of A-SnO_2@PCNS (Figure 1i, Manuscript).

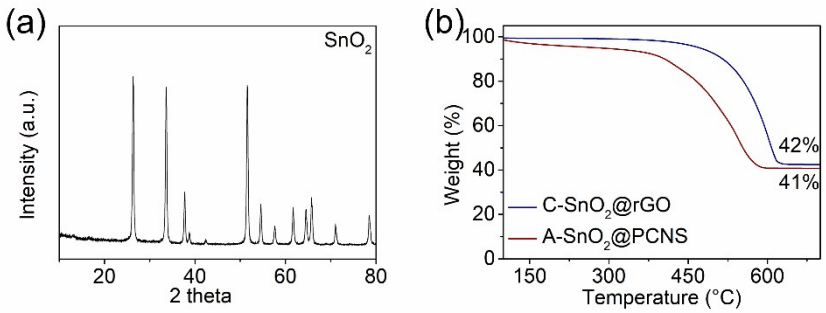

Figure S4. (a) XRD pattern of commercial SnO_2 nanoparticles. (b) TGA profiles of C-SnO_2@rGO and A-SnO_2@PCNS pyrolyzed in the air atmosphere.

The XRD pattern of commercial SnO_2 nanoparticles showed intensed characteristic peaks of a crystalline rutile SnO_2 phase, indicating the high crystallinity. Based on the TGA profiles in air atmosphere, the weight content of SnO_2 in C-SnO_2@rGO and A-SnO_2@PCNS were determined to be approximately 42 and 41 wt.%, respectively.

Table S1. Pore structure parameters for the carbon materials.

	S_{BET} [a]	V_t [b]	Specific surface area[c] ($m^2 g^{-1}$)		Pore volume[d] ($cm^3 g^{-1}$)	
	($m^2 g^{-1}$)	($cm^3 g^{-1}$)	Micropore	Meso- and macropore	Micropore	Meso- and macropore
HPCNS	319.3	0.241	249.6	69.7	0.112	0.129
A-SnO_2@PCNS	69.4	0.124	18.6	50.8	0.008	0.116
C-SnO_2@rGO	66.4	0.115	5.5	60.9	0.002	0.113
HPCNS-800	319.5	0.423	44.8	274.7	0.021	0.402
C-SnO_2@PCNS-800	168.4	0.384	2.7	165.7	0.004	0.380
C-SnO_2@PCNS-2.4	50.9	0.126	8.9	42.0	0.003	0.123

[a] The total specific surface area was calculated by Brunauer-Emmett-Teller (BET) method.

[b] The total pore volume was determined at a relative pressure of 0.98.

[c] The specific surface area of micropores and mesopores were calculated by t-plot method.

[d] The pore volume of micropores was calculated by t-plot method.

It should be noted that the pore structure of GO was difficult to determine since the degas process at temperature over 200 °C would lead to the elimination of some oxygen functional groups in GO.

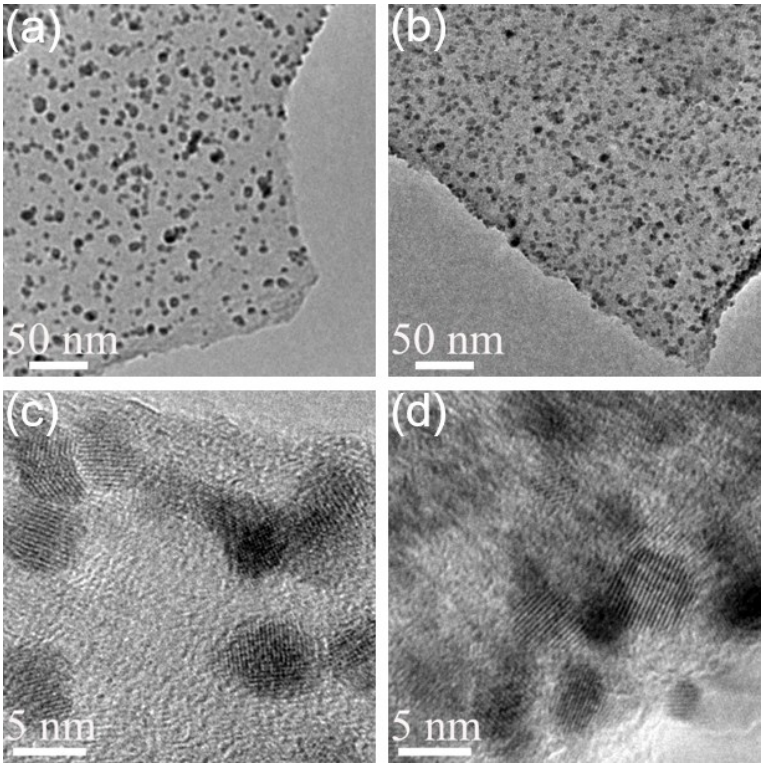

Figure S5. TEM images of (a) C-SnO_2@PCNS-800 and (b) C-SnO_2@PCNS-2.4. HRTEM images of (c) C-SnO_2@PCNS-800 and (d) C-SnO_2@PCNS-2.4.

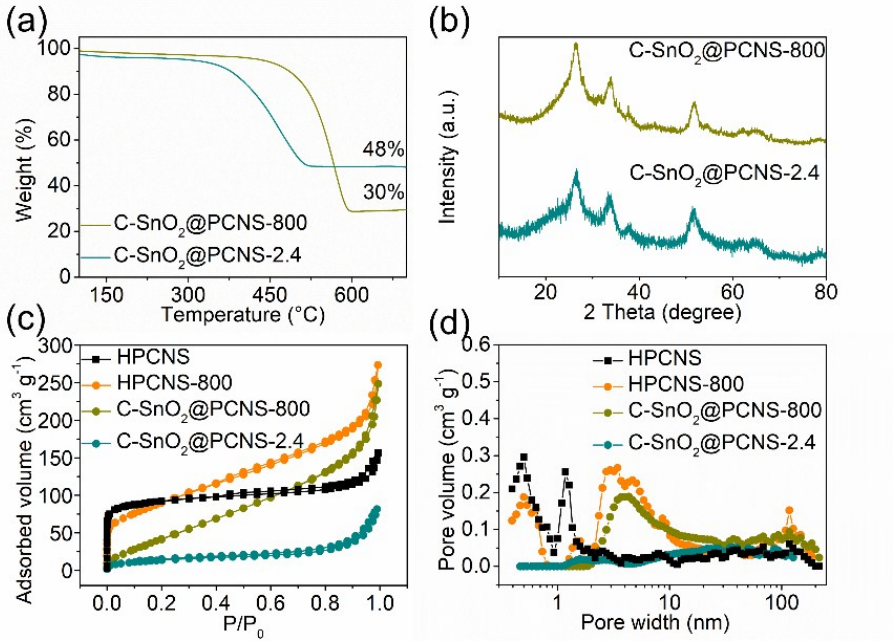

Figure S6. (a) TGA profiles of C-SnO_2@PCNS-800 and C-SnO_2@PCNS-2.4 pyrolyzed in air atmosphere. (b) XRD patterns, (c) nitrogen adsorption-desorption isotherms and (d) pore-size-distribution plots of C-SnO_2@PCNS-800 and C-SnO_2@PCNS-2.4.

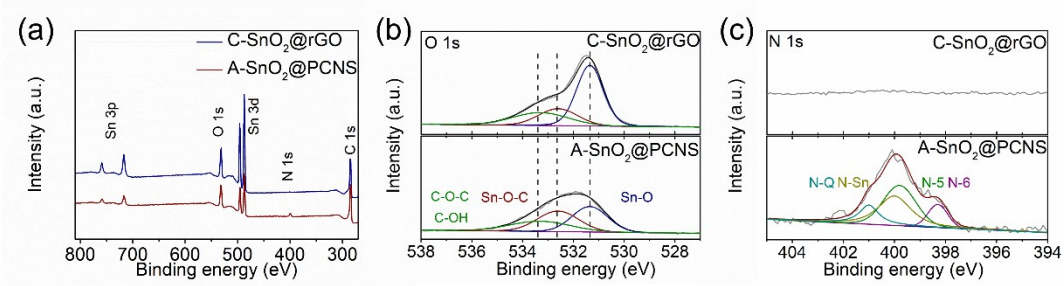

Figure S7. (a) XPS spectra of C-SnO_2@rGO and A-SnO_2@PCNS. High-resolution XPS spectra of (b) O 1s and (c) N 1s.

The high-resolution O1s XPS spectra for all the samples were deconvoluted into three individual component peaks as follows: Sn-O (531.6 eV), Sn-O-C (532.6 eV) and C-OH/C-O-C (533.3 eV).[5] The high-resolution N1s XPS spectra for all the samples were deconvoluted into four individual component peaks as follows: Sn-N-C (400.0 eV), pyridinic-N (N-6, 398.2 eV), pyrrolic-N (N-5, 399.9 eV) and quaternary-N (N-Q, 401.0 eV).[3, 4] The binding energies of Sn $3d_{5/2}$ and Sn $3d_{3/2}$ for C-SnO_2@rGO was 487.6 and 496 eV, respectively, implying that Sn existed only in the 4+ state.[5]

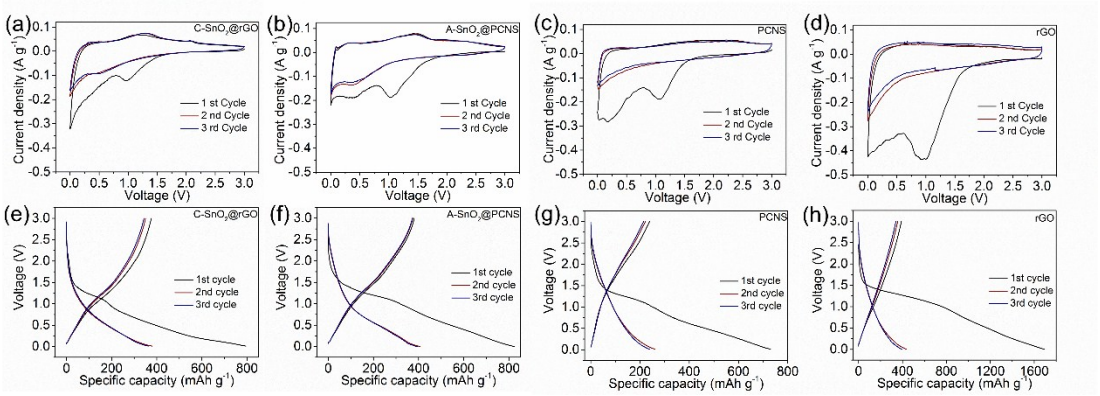

Figure S8. CV curves of (a) C-SnO_2@rGO, (b) A-SnO_2@PCNS, (c) PCNS and (d) rGO anodes at the scan rate of 0.1 mV s^{-1}. GCD curves of (e) C-SnO_2@rGO, (f) A-SnO_2@PCNS, (g) PCNS and (h) rGO anodes at the current density of 0.05 A g^{-1}.

C-SnO_2@rGO and A-SnO_2@PCNS anodes exhibited similar anodic and cathodic peak positions at small scan rates, corresponding to the similar Na-ion storage reactions. Specifically, the cathodic peaks in first discharge process at 1.0 V were due to the formation of solid electrolyte interphase (SEI) and irreversible reductive reactions between SnO_2 and Na ions that formed Na_2O and Sn.[6] The cathodic peaks at 0.4 V resulted from the formation of NaSn and Na_9Sn_4, while the cathodic peaks at 0.01 V corresponded to the formation of $Na_{15}Sn_4$ as well as the Na-ion storage by carbon supports.[7, 8] In the charge process, the anodic peaks at 0.25 and 1.4 V were associate with the reversible dealloying of Na_xSn.[9] It should be noted that the supports might also contribute irreversible capacities in the first discharge process (Figure S8c, d), leading to the relatively low coulombic efficiencies of C-SnO_2@rGO and A-SnO_2@PCNS anodes.

At the current density of 0.05 A g^{-1}, PCNS and rGO anodes exhibited much lower initial coulombic efficiencies than C-SnO_2@rGO and A-SnO_2@PCNS anodes. Numerous pores and surface O-containing functional groups contributed large irreversible capacities to PCNS and rGO anodes, respectively. After SnO_2 loading, most of the pores and surface O-containing functional groups were filled by SnO_2 and bonded with SnO_2, respectively. Thus, the irreversible capacities decreased obviously. Moreover, the CV and GCD curves also showed that C-SnO_2@rGO and A-SnO_2@PCNS anodes exhibited lower sodiation/desodiation potentials than PCNS and

rGO anodes. The capacities of PCNS and rGO anodes were primarily contributed by the reversible reactions between O heteroatoms and Na ions at high potentials (>1.0 V). After SnO_2 loading, the O heteroatoms was bonded with SnO_2 that exhibited capacities at relatively low potentials (<1.5 V). Thus, C-SnO_2@rGO and A-SnO_2@PCNS were better than PCNS and rGO as anodes for Na-ion storage.

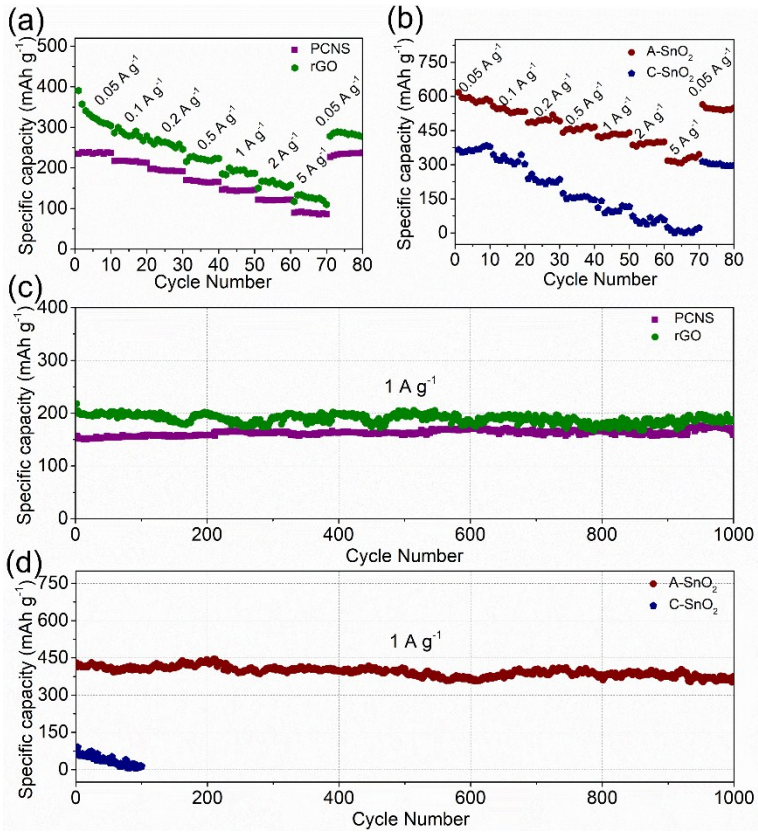

Figure S9. (a) Rate capacities of rGO and PCNS anodes at various current densities from 0.05 to 5 A g^{-1}. (b) Rate capacities of C-SnO_2 and A-SnO_2 anodes at various current densities from 0.05 to 5 A g^{-1}. (c) Cycling performance of rGO and PCNS anodes at 1 A g^{-1}. (d) Cycling performance of C-SnO_2 and A-SnO_2 anodes at 1 A g^{-1}. All the specific capacities for the electrodes were charge capacities.

The capacity of C-SnO_2 or A-SnO_2 anode (C_{SnO_2}) was calculated based on the weight of C-SnO_2 or A-SnO_2 alone according to the equation below:

$$C_{SnO_2} = \left(C_{SnO_2@S} - \omega_S \times C_S\right)/(1 - \omega_S)$$

where $C_{SnO_2@S}$ is the measured capacity of C-SnO_2@rGO or A-SnO_2@PCNS, C_S is the measured capacity of support (rGO or PCNS), ω_S is the weight percent of support (rGO or PCNS) in the composites.

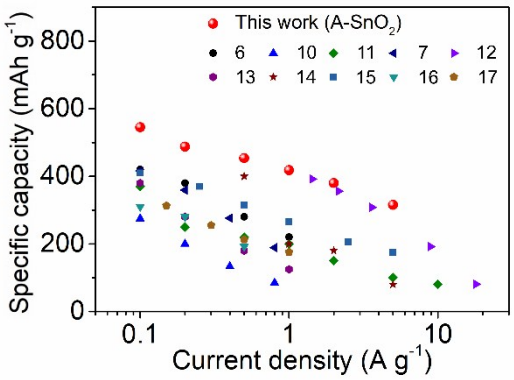

Figure S10. Rate capability comparison with other works about SnO_2 anodes for Na-ion storage.[6, 7, 10-17]

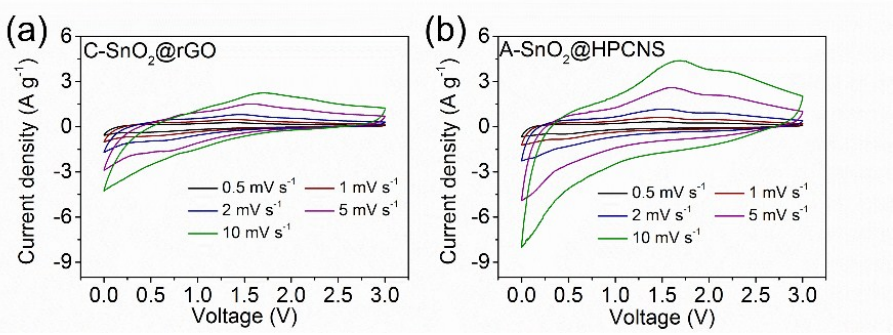

Figure S11. CV curves of (a) C-SnO_2@rGO and (b) A-SnO_2@PCNS anodes at various scan rates from 0.5 to 10 mV s^{-1}.

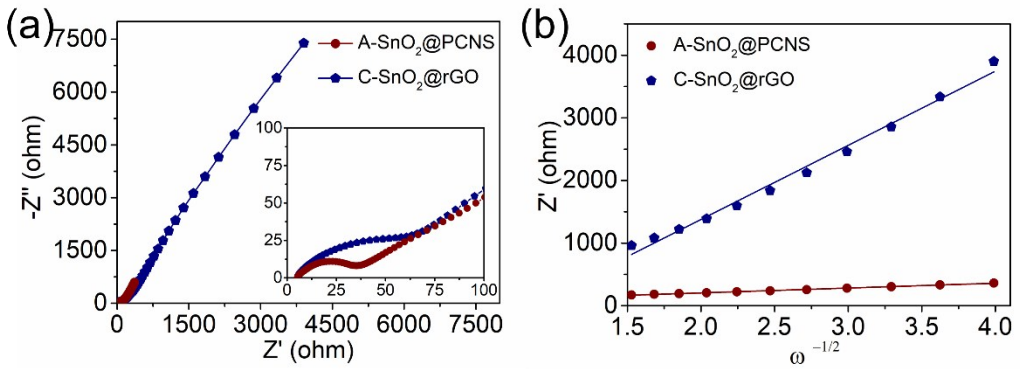

Figure S12. (a) Nyquist plots for C-SnO_2@rGO and A-SnO_2@PCNS anodes (inset: enlarged view of high and middle frequency regions). (b) Dependence of Z' on the reciprocal square root of the angular frequency for C-SnO_2@rGO and A-SnO_2@PCNS anodes in low frequency regions. GITT curves and the corresponding D_{Na^+} in discharged and charged states for (c) C-SnO_2@rGO and (d) A-SnO_2@PCNS anodes.

Table S2. Simulation results of the kinetic parameters of A-SnO_2@PCNS and C-SnO_2@rGO anodes.

	R_e (Ω)	R_f (Ω)	R_{ct} (Ω)	σ
A-SnO_2@PCNS	5.7	10.6	23.6	78
C-SnO_2@rGO	5.9	13.4	61.8	1185

The Nyquist plots shown in Figure S12a were fitted according to our previous work.[1] The simulated results of electrolyte impedance (R_e), SEI resistance (R_f) and charge-transfer resistance (R_{ct}) were shown in Table S2. The Warburg factors (σ) were determined by the linearly fitting the Z' versus $\omega^{-1/2}$ plots (Z' is the real parts of the complex impedance Z, and ω is the angular frequency which is given by $\omega = 2\pi f$). [3]

GITT measurements were performed under a constant current pulse of 20 mA g^{-1} for 30 minutes and a relaxation process over 2 hours. The sodium diffusion coefficient (D) was calculated from the GITT potential profiles by Fick's second law with the following equation:[18]

$$D = \frac{4}{\pi\tau}\left(\frac{m_B V_m}{M_B S}\right)^2\left(\frac{\Delta E_S}{\Delta E_t}\right)^2$$

Where τ and t are the relaxation time (s) and the duration of the current pulse (s); m_B is the active mass of the electrodes (g); S (cm^2) is the geometric area of the electrodes. ΔE_S (V) is the quasi-thermodynamic equilibrium potential difference before and after the current pulse; ΔE_t (V) is the potential difference during current pulse. The value of V_m/M_B can be obtained from the density of composites.

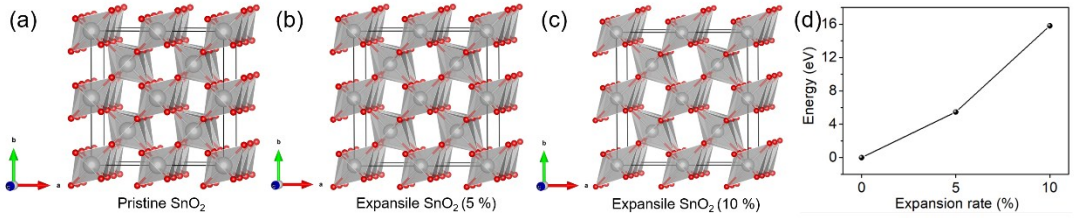

Figure S13. (a-c) Optimized SnO_2 2×2×2 supercells with different expansile rates (red and gray balls in the supercells corresponding to O and Sn atoms, respectively). (d) The relative energy for optimized SnO_2 structures with different expansile rates.

As shown in Figure S13d, the expansile SnO_2 structure was more unstable than the pristine SnO_2 structure. However, the formation of A-SnO_2 in A-SnO_2@PCNS became feasible by virtue of the micropore confinement and abundance of chemical bonds between SnO_2 and the carbon support.

Table S3. The bond lengths of Sn-O and Sn-Sn in optimized SnO_2 structures with different expansile rates based on DFT results, A-SnO_2 structure within A-SnO_2@PCNS and C-SnO_2 structure within C-SnO_2@Rgo based on EXAFS results.

	6 coordination Sn-O (Å)	2 coordination Sn-Sn (Å)	8 coordination Sn-Sn (Å)
Pristine SnO_2 (cal.)	2.09	3.24	3.78
SnO_2 with 5 % expansion (cal.)	2.13	3.28	4.00
SnO_2 with 10 % expansion (cal.)	2.10	3.21	4.27
C-SnO_2 within C-SnO_2@rGO (exp.)	1.69	2.50	3.00
A-SnO_2 within A-SnO_2@PCNS (exp.)	1.69	2.55	3.12

As shown in Table S3, A-SnO_2@PCNS showed similar change tendency of bond lengths with the SnO_2 structures (5 % expansile rate), indicating that the SnO_2 mode with 5 % expansile rate was suitable for A-SnO_2@PCNS.

Table S4. Energy of per formula unit for SnO_2, Na_2O, Sn with different space groups based on DFT calculations.

	Space group	Z	Supercell	Total energy (eV)	Energy per formula unit (eV)
SnO_2	$P4_2mnm$	2	2×2×2	-300.32	-18.77
Na_2O	Fm**Error!**m	4	1×1×1	-45.37	-11.34
	Fd**Error!**ms	8	1×1×1	-30.65	-3.83
Sn	I4mmm	2	1×1×1	-7.60	-3.80
	I41amds	4	1×1×1	-15.13	-3.78
	Im**Error!**m	2	1×1×1	-7.58	-3.79

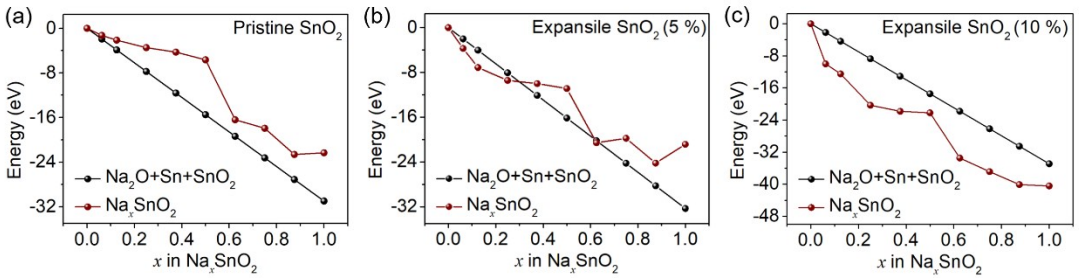

Figure S14. The formation energy of intermediates based on different storage mechanism during the sodiation processes of (a) pristine SnO_2, (b) SnO_2 with 5 % expansion and (c) SnO_2 with 10 % expansion (black and red points were determined by conversion reaction and intercalation reaction, respectively).

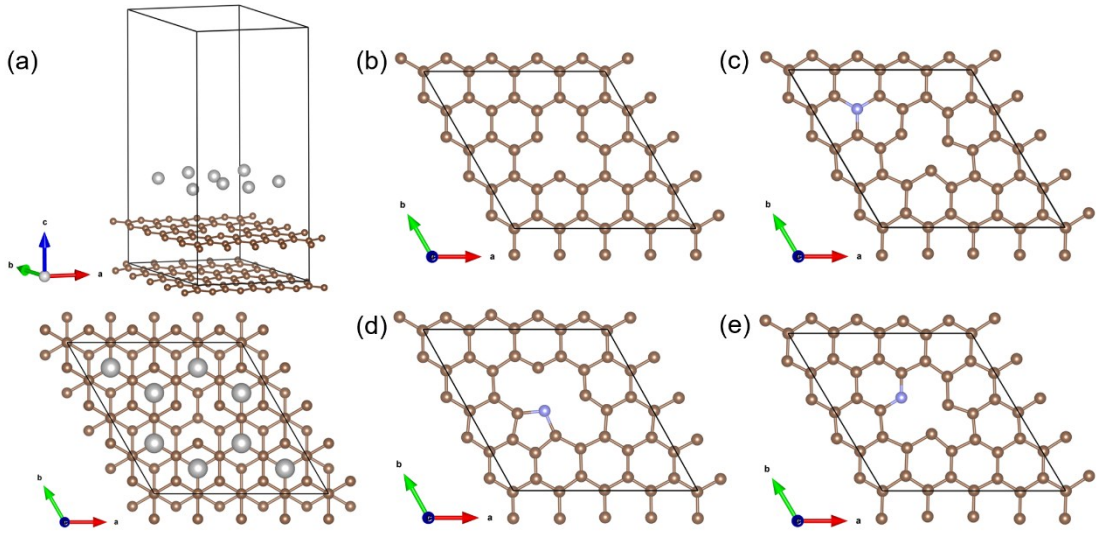

Figure S15. (a) Optimized interface structures of defect graphene (4×4 supercell) and Sn surface (8 Sn atoms on the defect graphene). Defect graphene modes (b) without N doping and with (c) graphitic N, (d) pyridinic N and (e) pyrrolic N doping.

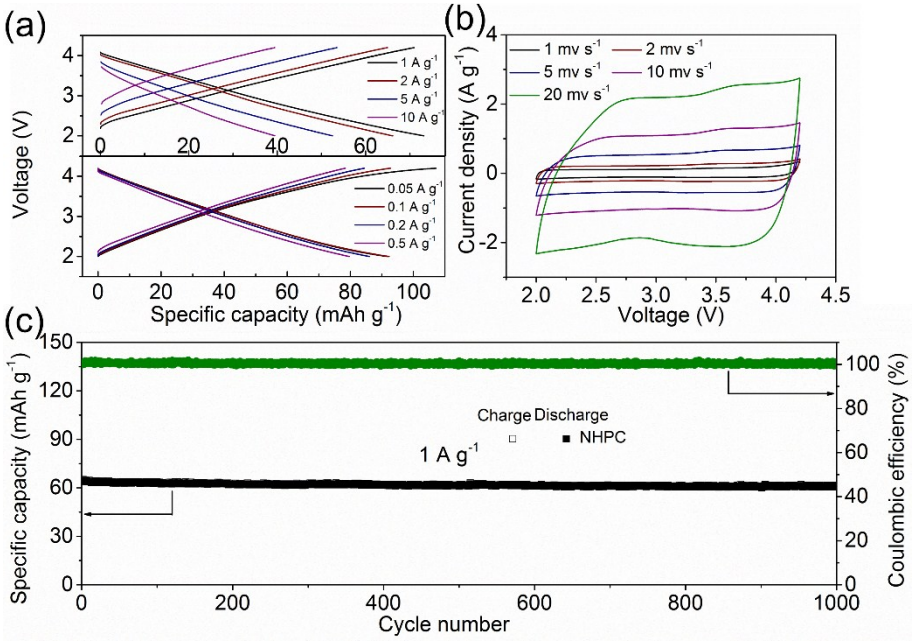

Figure S16. Electrochemical performance of HPC cathode. (a) Galvanostatic charge-discharge curves at different current densities. (b) CV curves at various scan rates from 1 to 20 mV s^{-1}. (c) Cycling performance at the current density of 1 A g^{-1}.

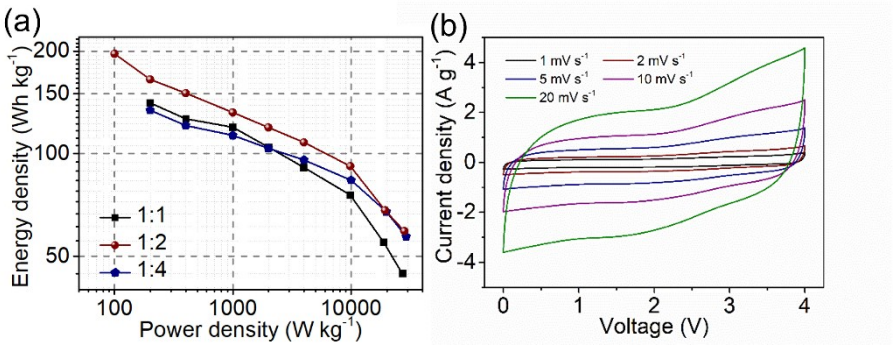

Figure S17. (a) The Ragone plots of A-SnO_2@PCNS||HPC NICs using different mass ratios of cathode to anode materials. (b) The CV curves of A-SnO_2@PCNS||HPC NIC at various scan rates from 1 to 20 mV s^{-1}.

References:

1. J. Niu, S. Zhang, Y. Niu, H. Song, X. Chen, J. Zhou and B. Cao, *J. Mater. Chem. A*, 2015, **3**, 19892-19900.
2. D. He, J. Niu, M. Dou, J. Ji, Y. Huang and F. Wang, *Electrochim. Acta*, 2017, **238**, 310-318.
3. J. Niu, J. Liang, R. Shao, M. Liu, M. Dou, Z. Li, Y. Huang and F. Wang, *Nano Energy*, 2017, **41**, 285-292.
4. S. Pan, C. Ye, X. Teng, H. Fan and G. Li, *Appl. Phys. A*, 2006, **85**, 21-24.
5. W. Chen, K. Song, L. Mi, X. Feng, J. Zhang, S. Cui and C. Liu, *J. Mater. Chem. A*, 2017, **5**, 10027-10038.
6. J. Patra, H.-C. Chen, C.-H. Yang, C.-T. Hsieh, C.-Y. Su and J.-K. Chang, *Nano Energy*, 2016, **28**, 124-134.
7. Y.-X. Wang, Y.-G. Lim, M.-S. Park, S.-L. Chou, J. H. Kim, H.-K. Liu, S.-X. Dou and Y.-J. Kim, *J. Mater. Chem. A*, 2014, **2**, 529-534.
8. R. S. Kalubarme, J.-Y. Lee and C.-J. Park, *ACS applied materials & interfaces*, 2015, **7**, 17226-17237.
9. Z. Huang, H. Hou, G. Zou, J. Chen, Y. Zhang, H. Liao, S. Li and X. Ji, *Electrochim. Acta*, 2016, **214**, 156-164.
10. L. Fan, X. Li, B. Yan, J. Feng, D. Xiong, D. Li, L. Gu, Y. Wen, S. Lawes and X. Sun, *Adv. Energy Mater.*, 2016, **6**, 1502057.
11. Z. Li, J. Ding, H. Wang, K. Cui, T. Stephenson, D. Karpuzov and D. Mitlin, *Nano Energy*, 2015, **15**, 369-378.
12. M. Dirican, Y. Lu, Y. Ge, O. Yildiz and X. Zhang, *ACS applied materials & interfaces*, 2015, **7**, 18387-18396.
13. A. Jahel, C. M. Ghimbeu, A. Darwiche, L. Vidal, S. Hajjar-Garreau, C. Vix-Guterl and L. Monconduit, *J. Mater. Chem. A*, 2015, **3**, 11960-11969.
14. H. Bian, X. Xiao, S. Zeng, M.-F. Yuen, Z. Li, W. Kang, Y. Denis, Z. Xu, J. Lu and Y. Y. Li, *J. Mater. Chem. A*, 2017, **5**, 2243-2250.
15. J. Qin, N. Zhao, C. Shi, E. Liu, F. He, L. Ma, Q. Li, J. Li and C. He, *J. Mater. Chem. A*, 2017, **5**, 10946-10956.

16. Y. C. Lu, C. Ma, J. Alvarado, T. Kidera, N. Dimov, Y. S. Meng and S. Okada, *J. Power Sources*, 2015, **284**, 287-295.
17. Y. Zhao, C. Wei, S. Sun, L. P. Wang and Z. J. Xu, *Adv. Sci.*, 2015, **2**, 1500097.
18. B. Cao, Q. Zhang, H. Liu, B. Xu, S. Zhang, T. Zhou, J. Mao, W. K. Pang, Z. Guo and A. Li, *Adv. Energy Mater.*, 2018, **8**, 1801149.